ETH zürich

ETH Library

The chain of processes forming porphyry copper deposits

Electronic Appendix

Dataset

Author(s):
Heinrich, Christoph A.

Publication date:
2024-02

Permanent link:
https://doi.org/10.3929/ethz-b-000657809

Rights / license:
Creative Commons Attribution 4.0 International

Originally published in:
Economic Geology

This page was generated automatically upon download from the ETH Zurich Research Collection.
For more information, please consult the Terms of use.

Electronic Appendix[1] to

The chain of processes forming porphyry copper deposits

published by *Economic Geology*, 2024, Open Access at doi:10.5382/econgeo.5069

Christoph A. Heinrich
Department of Earth Sciences, ETH Zurich
Faculty of Mathematics and Natural Science, University of Zürich
Clausisusstrasse 25, 8092 Zürich, Switzerland
heinrich@erdw.ethz.ch

I. Lithosphere Preparation and Melt Generation

Mo, Cu and Au endowment in porphyry-type ore deposits

Data for Figure 2 were taken from Mutschler et al. (1999) with additional points for major Mo ± Cu deposits in Asia listed by Gao et al. (2018). For points along the left axis, no Cu data were reported.

Figure 3 comparing Au and Cu endowments of porphyry deposits uses the compilation by Chiaradia (2020), which is mainly based on Singer et al. (2008). Total tonnages deviate from other compilations (including the most recent download from https://mrdata.usgs.gov/porcu/) more than reported ratios of Cu/Au grade, so that Au tonnages for El Teniente and Escondida were corrected to the Cu/Au ratio reported by Cooke et al. (2005). Otherwise Figure 3 only differs from the diagram reproduced in Park et al. (2021) by the logarithmic scale and the emphasis of province-scale variation of Cu/Au ratios using selected symbol colors.

The stippled line shows the approximate total in-ground value of 100b $US assuming long-term metal prices of 5000 US$/t Cu (Sykes and Trench, 2014) and 900 $US/oz Au (http://minexconsulting.com/wp-content/uploads/2019/04/NewGenGold-2013-R-Schodde-paper.pdf), averaged between 1974 and 2013.

Some notes on Mo geochemistry and two major Mo ore provinces

Molybdenum is a common by-product of porphyry Cu deposits worldwide, but there is a striking global provinciality of two distinct Mo-dominant regions in the Western USA and in Northern China. Both are underlain by subcontinental mantle lithosphere that was modified by subduction processes during the Paleoproterozoic. The global process that led to these two major metal anomalies have hardly been discussed, inviting some speculation.

Molybdenum valency is +VI in aqueous solutions from surface waters (Kendall et al., 2017) to magmatic-hydrothermal fluids (Seo et al., 2012; Sun et al., 2014). In crustal igneous rocks, a significant fraction is present as Mo(VI) in Ti-rich oxide minerals (rutile, ilmenite, magnetite) and titanite, besides a variable rest as Mo(IV) in accessory molybdenite, while other sulfides are generally Mo-poor (Greaney et al., 2018; Li et al., 2020). As a result of the transfer of Mo(VI) to the magmatic volatile phase, upper-crustal granitic rocks (1.1 ppm Mo; Rudnick and Gao, 2014), are depleted by ~60% compared with Mo concentrations expected from magmatic processes alone, based on abundances of elements with similar degree of incompatibility (Greaney et al., 2018). Conversely, high-silica and highly potassic granitic melt inclusions giving rise to major Mo deposits are selectively enriched in Mo up to 5-10ppm, rising to 40ppm in highly Cs-enriched late fractionates (Lerchbaumer and Audétat, 2013). Mo-mineralizing granitic magmas are geochemically specialized (White et al., 1981; Carten et al., 1993; Seedorff et al., 2005) but whether their parental melts were already Mo-enriched, and whether they originate in the lower crust or upper mantle, remains debated (Westra and Keith, 1981; Bookstrom et al., 1988).

Mo isotope ratios are used for studying earth surface systems (Archer and Vance, 2008; Arnold et al., 2012; Westermann et al., 2014; Kendall et al., 2017), showing secular variations in black shales (Scott et

---

[1] This Appendix is available at ETH Research Collection, https://doi.org/10.3929/ethz-b-000657809

al., 2008; Large et al., 2014), and in bulk crust or mantle reservoirs (Ahmad et al., 2022; Hin et al., 2022) including igneous rocks from arcs and ore-forming systems (Hannah et al., 2007; Breillat et al., 2016; Wille et al., 2018; Mao et al., 2023).

The geochemical behavior of Mo in global rock reservoirs, seawater and reduced sediments is consistent with the tentative speculation that the beginning of oxidative weathering on the continents initiated a period of exceptionally high riverine Mo flux to the oceans, which was sequestered in widespread anoxic bottom sediments. These represented a relatively concentrated Mo reservoir available for subsequent subduction. More restricted anoxia in subduction trenches after further oxygenation of the ocean may have led to a period in the Paleoproterozoic with higher concentration of Mo in locally restricted sediments, e.g. in deep-see trenches. Such sediments are likely to be subducted and have low chance of preservation in the geological record. Their subduction may have led to a period of particularly efficient transfer of Mo to the overlying mantle wedge around ~1.8 Ga. This approximate age is indicated by Pb isotope modeling for Bingham Cu-Mo-Au deposit (Pettke et al., 2010) and is consistent with the unusually radiogenic isotope geochemistry of other SW-USA mantle magmas (Farmer and De Paolo, 1984). Some pre-enrichment of the mantle below SW-USA in the area of the giant climax-type Mo deposits is indicated by anomalously Mo-rich rocks of mantle-derived alkali-basaltic to crustal felsic composition in the SW-USA formed after 1.7 Ga (Westra and Keith, 1981; Bookstrom et al., 1988). It is tempting to consider a period of Mo-enrichment in parts of the ancient lithosphere shortly after the Great Oxidation Event as an oceanic counterpart to the advent of hydrothermal U deposits on the continents around the same time period (Cuney, 2010).

II. Lower-Crustal Fractionation to a Fertile Magma

The role of magmatic sulfides in generating fertile magmas

Magmatic sulfides, as liquid Cu-Ni-Fe sulfide melt, as Cu-rich intermediate sulfide solid solution (ISS) or as Fe-rich monosulfide solid solution (MSS), are highly element-selective hosts to Cu, Au and other metals in magmatic-hydrothermal ore deposits. Given the high and selective partition coefficients for chalcophile ore metals between sulfide phases, silicate melt and hydrothermal fluid, it would seem fortuitous that accessory deep sulfides are always at the balance between being detrimental or favorable for ore formation (cf. Du and Audétat, 2020). More likely, their role in generating windows towards fertile magmas is still insufficiently understood (e.g., by relatively late saturation in moderately S-rich but highly oxidised conditions, followed by their entrainment in fractionated melts; cf. Lee and Tang, 2020). This ambiguity partly relates to inherent limitations of all rock-based observations: sulfides preserved in lower-crustal xenoliths by nature are not those that contributed to ore formation, and magmatic rocks preserved at the surface do not represent magmas prior to fluid saturation at the typical pressure where ore fluids are generated. For example, the zircon record of porphyry intrusions associated with ore formation at Bingham Canyon indicates monotonous fractionation of a relatively homogeneous monzonitic magma reservoir driving large-scale hydrothermal fluid generation (Large et al., 2021). This seems to conflict with rare melanonephelinitic dikes that were found in the mine (Hattori and Keith, 2001), and with volcanic rocks exposed outside the mine area. Samples of the latter variably indicate injection of mafic magmas and mafic – felsic magma mixing involving magmatic sulfides but unspectacular bulk Cu content of the magmas (Zhang and Audétat, 2017), or magmas of intermediate composition but unusually high Cu content (Grondahl and Zajacz, 2017). The resolution of such conflicting evidence probably relates to processes occurring at different scales and times, including local variations in the degree of sulfide – silicate separation leading to variations in modal sulfide abundance, which in turn has a sensitive influence on the extent of sulfide decomposition and Cu loss after hydrothermal fluid saturation (Chelle-Michou and Rottier, 2021; Heinrich and Connolly, 2022).

An integrated 66% Cu deficit in volcanic rocks of thick-crust continental arcs compared to thin-crust oceanic arcs was estimated by Chiaradia (2014, supplementary figure S2). Explaining this by Cu loss to sulfide-rich cumulates in the lower crust is consistent with published interpretations of Au and PGE data and slight enrichment of Cu in preserved lower-crustal cumulates (Richards, 2011; Cocker et al., 2015; Park et al., 2021). However, major Cu loss precisely in areas where the best Cu deposits occur seems counter to my intuition. Decomposition of entrained magmatic sulfides with transfer of Cu to the fluid may provide an alternative explanation of the observed Cu deficit in preserved thick-arc volcanics

(Heinrich and Connolly, 2022; see also Appendix IV). Published suggestions how subsequent processes in the chain towards ore formation compensate for an initial deep-crustal Cu loss are unspecific or contradictory. Thus, accumulated sulfides from a drier and more reducing melt stage might be redissolved by a later stage of more oxidized and more hydrous melting at depth, but the reason for the required change in melting conditions and the physical process of collecting dispersed sulfide from older cumulates have not been explained by advocates of such 'remobilization' (Wilkinson, 2013; Rezeau and Jagoutz, 2020). Moreover, relatively cool arc systems are dominated by solid iron sulfide (MSS), which would predict preferential loss of Cu and increasing Au/Cu in the silicate melt (Du and Audétat, 2020; Li et al., 2021), counter to the observation that the largest deposits of the central Andes have low Au/Cu. Observations of Kohistan cumulates indicate former liquid as well as solid sulfide, and their analysed metal ratios have been modeled to suggest almost complete removal of precious elements including Au, but only of ~40% of available Cu (Ahmad et al., 2021). Independent observations and melting experiments come to the opposing conclusion that remelting such cumulates will not yield the expected magma compositions (Du and Audétat, 2020; Zhang et al., 2022). In general, pre-enrichment of bulk Cu concentration of source rocks by increasing the modal proportion of sulfides will not lead to more Cu-rich silicate melts during later melting, if sulfide solubility is limited at given P-T-fO_2 conditions. On the other hand, increasing the total Cu content at a constant quantity of mantle sulfide (e.g., by subduction metasomatism prior to partial melting of the mantle wedge; Ague et al., 2022) would favor Cu-enrichment in a later silicate melt. At this stage of understanding, I question the assertion that the initial ore metal concentrations of mantle melts on the way to great porphyry deposits is necessarily the same as in average mantle basalt.

III. Magma Ascent and Volume of Mineralizing Reservoirs

Mass and volume estimates to generate a 100Mt Cu deposit

Figure 4 shows alternative processes of magma emplacement, fractional crystallization and fluid production for a Cu-rich hydrous basaltic magma capable of accumulating 100 Mt Cu in an orebody with 1% Cu ore. All three cartoons are scaled to illustrate approximate minimum volumes of magma (sum of pink and green boxes, identical in each cartoon), melt (pink), crystals (green; cumulate plus suspended phenocrysts) and fluid (blue; superimposed on the melt volume from which it is expelled). The geometry of all cartoons is circular (cylindrical) with the same horizontal (radius) and vertical scales (depth below surface). The assumed 'footprint' with a radius r = 6 km at the base of the system is arbitrary and common to all three cartoons.

The vertical positions of melt volumes are chosen to be consistent with the P-dependence of H_2O solubility in silicate melts (Baker and Alletti, 2012) but ignore petrological details. The density of magmatic silicate materials is assumed to be 2800 kg m^{-1} (Loucks, 2021), ignoring differences between crystals and silicate melts and their dependence on P, T and composition. I only consider the density variation of magmatic H_2O fluid with changing P, at an assumed T = 850°C (Haar et al., 1984; Weingärtner and Franck, 2005; calculated with 'SoWat' by Driesner, 2007). 100ppm Cu and 3 wt% H_2O in the initial hydrous basalt melt are assumed to behave perfectly incompatibly, i.e., silicate crystals fractionating to cumulates are H_2O and Cu-free. No melt, H_2O or Cu is added from or lost to the surrounding crust. All other chemical components are ignored, including CO_2 which leads to fluid saturation at higher P, but is much less abundant, so that H_2O dominates component transfer between hydrous magma and fluid, including the stability of magmatic sulfides (see digital Supplement to Heinrich and Connolly, 2022). 100 Mt $= 10^8$ t Cu initially contained in a hydrous basalt melt with a concentration of 100 ppm Cu requires 10^{12} t basalt occupying ~360 km^3. This is shown by the sum of green and pink rectangles (cylindrical disks), identical in all 3 cartoons. Disk heights h are calculated from cylinder volume $V_{cylinder} = \pi \cdot r^2 \cdot h$. For an assumed radius r = 6 km, the total basalt magma occupies a cylindrical disc with a vertical height of h = 3.16 km.

In Fig. 4A, the basalt volume is assumed to fractionate in the lower crust, separating into 75% minerals (a cumulate layer of 0.75 • 3.16 km = 2.37 km height; green) and 25% residual melt (a 0.79km high disk representing a volume of 90 km^3; stippled red line). This melt contains all the Cu (400ppm) and H_2O (12wt%). H_2O solubility in melt according to Baker and Alletti (2012) requires a pressure of >600 MPa or a depth of >22km, which is chosen as the base of the melt body in Fig. 4A. Thus, the deep (~ granitic)

melt in the lower crust is at the verge of fluid saturation. To illustrate the scenario of direct ascent of all this melt through a pipe or dike to the point of potential ore formation (assumed at 5km below surface; red sphere), the melt volume was recalculated to a cylinder with 22 – 5 = 17km height yielding a radius r = 1.30 km (diameter 2.60km). The ascending and decompressing magma saturates fluid immediately at all depths, and the volume of fluid produced in each depth interval was calculated from H_2O density (e.g., ~710kgm^{-3} at 21km, ~540kgm^{-3} at 12km, ~290kgm^{-3} at 5km) and expressed as depth-dependent cylinder radius (0.9km, 1km, 1.4km, respectively). This fluid volume contribution is superimposed with blue pattern on the pink magma cylinder, to emphasise that the exsolved fluid mostly occupies extra space because the volume of fluid is much larger than the volume decrease upon crystallizing hydrous melt to solid rock (e.g., Malfait et al., 2014).

Fig. 4B shows the same total magma volume distributed over randomly chosen smaller disks. The distinction into crystal and melt volumes is arbitrary, to indicate composition-dependent fluid generation in smaller isolated batches at all depths, as increasingly fractionated melt percolates through bigger or smaller reservoirs of magma mush.

Fig. 4C assumes that the initial lower-crustal magma chamber (Fig. 4A) separates only 50% crystals to generate a partly fractionated (e.g., dioritic or monzonitic) melt, which accordingly is only 2x enriched in Cu (200ppm) and H_2O (6 wt%). This melt is injected through a thin channelway (volume ignored) into an upper-crustal magma chamber. Thereby it stays fluid-undersaturated until it reaches ~7km depths, corresponding to 6 wt% H_2O saturating at P ~200 MPa (Baker and Alletti, 2012). This depth is chosen as top of the upper-crustal melt volume, which will gradually expel its entire H_2O as fluid of intermediate density (~ 400 kg m^{-3}), controlled by cooling and crystallization of the magma.

IV. Transfer of Ore Components from Melt to Fluid

Calculation method for Rayleigh fractionation

Figure 5 describes the principles of model calculations for the stepwise transfer of hypothetical elements 'blue', 'gray' and 'red' from hydrous silicate melt to aqueous fluid, assuming constant D_{blue}, D_{gray} and D_{red}. Open-system fractionation or Rayleigh distillation assumes that after each step of crystallization, the exsolved fluid batch leaves the system and does not equilibrate or mix with later fluid batches. Calculations follow the approach and equations in Audétat (2019) and were computed with the attached Excel file, setting distribution coefficients to be constant. This allows direct calculation of each step from the previous state of the system.

Figure 6 uses experimental D values that vary for Cl, Cu and Mo as a function of pressure, SiO_2 content of the silicate melt and the Cl/H_2O ratio in the system. Equations and parameterizations of D are taken from Tattitch and Blundy (2017) and Tattitch et al. (2021). Results were back-checked to example calculations in Tattitch et al. (2021), to confirm my approach to iterative solution by stepwise SOLVER calculations in Excel. The empirical dependence of melt fraction from intermediate to silicic magma compositions (Tattitch et al., 2021; Supplementary figure 6) was graphically extrapolated to a hydrous basalt with ~50 wt% SiO_2, to estimate that 50% crystallization prior to fluid saturation will raise the SiO_2 concentration in the melt to ~62%. This value was assumed as point of initial fluid saturation in a hypothetical dioritic or monzonitic melt depicted in Figure 6C. Extrapolation to H_2O-undersaturated compositions is not strictly consistent with the published correlation between silica content and crystal fraction, but the argument made using Figures 6B and 6C is not sensitive to this simplification. The calculation is documented in four worksheets of the file *Cl-Cu-Mo-S-H2O-Extraction.xlsx* (also available at https://doi.org/10.3929/ethz-b-000657809) which were used to derive Figure 6A to D. Note that system compositions are rounded for the left text column in Figure 6 and refer to melt (not magma) compositions before fluid saturation.

The purpose of Figure 6 is to illustrate the effects of the depth of fluid generation and SiO_2 in melt on the behavior of Cl and ore metals in magmatic fluids. The four examples assume optimistic parameters, consistent with the minimal magma volumes needed for the formation of a giant porphyry Cu deposit in Figure 4. Predicted metal concentrations reach several wt% Cu, which is perhaps unrealistically high but still within the range of analysed fluid inclusion assemblages observed in several detailed studies (not only individual inclusions! Campos et al., 2006; Klemm et al., 2007; Landtwing et al., 2010; these data were perhaps prematurely disregarded as outliers caused by local redissolution of

earlier Cu-Fe sulfides or post-entrapment modification). The purpose of Figure 6 is not to assess the quantitative merit of predicted fluid compositions – cf. Tattitch et al. (2021). The multitude of observed concentrations in fluid inclusions (Kouzmanov and Pokrovski, 2012; varying over several magnitudes) not only include effects of post-entrapment modification but also of ore mineral precipitation. On the other hand, the stepwise extraction of fluid batches assumed in the Rayleigh fractionation model is not geologically realistic for a large magma reservoir, in which fluids are produced in different regions at variable degrees of crystallization and then partly mix *en-route* to the deposits, to an extent that is dependent on the hydrological mechanism of fluid extraction (Chelle-Michou et al., 2017; Fig. 7). Significant re-mixing on the magma reservoir scale is indicated by the observations in ore deposits that fluid inclusion salinity generally does not vary systematically with mineralization progress. A salinity and metal decrease with time would be expected from Figure 6B, for example, but such systematic variations with time have only been observed on local scale (e.g., miarolitic cavities in a small Adamello intrusion; Hennings et al., 2017).

Experimental uncertainties

All thermodynamic modeling, and particularly the decisive 'switchovers' contrasted by the four parts of Figure 6, are sensitive to significant experimental uncertainties in laboratory-measured data (e.g., Gion et al., 2022). They emphasize that such calculations should be used for depicting principal factors of influence rather than quantitative predictions to be compared to fluid inclusion analyses. Even the relation between wt% H_2O in silicate melt and P at fluid saturation (Baker and Alletti, 2012; Ghiorso and Gualda, 2015) is subject to greater uncertainty than the 5% relative pressure due to refitting of the second reference. Thus, the H_2O saturation pressure at 12 wt% H_2O is ~500 MPa according to the equation by Tattitch et al. (2021; used for Figure 6 for internal consistency), but ~600 MPa according to data review by Baker and Aletti (2012; as used for the depth scale in Figure 4 and in many other published papers), or ~800 MPa shown in Loucks and Fiorentini (2023a, using experimental data from Naney, 1983, to argue for super-wet granitic melts at the base of the crust).

The role of magmatic sulfides during fluid exsolution and metal transfer

On ascent to the upper crust, any entrained magmatic sulfides are decomposed upon saturation with H_2O-rich fluid (Mungall et al., 2015; Heinrich and Connolly, 2022). Progressive element fractionation during partial decomposition of magmatic sulfides and fluid extraction from crystallizing magmas has been modelled in several studies (e.g., Chelle-Michou and Rottier, 2021). Inclusions in phenocrysts of volcanic and subvolcanic rocks associated with porphyry Cu deposits indicate the presence of magmatic sulfides even in upper-crustal magmas (Hattori and Keith, 2001; Halter et al., 2005; Du and Audétat, 2020), consistent with at least partial entrainment of sulfide particles contributing to ore-metal enrichment (Wilkinson, 2013). Most sulfides observed in the matrix of upper-crustal magmatic rocks are largely decomposed to oxides (e.g., Larocque et al., 2000; Georgatou and Chiaradia, 2020). This occurs as soon as major aqueous fluid exsolution starts, thereby liberating S as well as chalcophile metals to the hydrothermal fluid. Varying partition coefficients between partly or completely decomposed magmatic sulfides (liquid or solid) can influence ore metal ratios in magmatic-hydrothermal fluids, which in turn affects the metal endowment of ore deposits (Halter et al., 2005; Nadeau et al., 2010; Edmonds and Mather, 2017; Rottier et al., 2020). Chelle-Michou and Rottier (2021) suggested based on quantitative fractionation modeling that the most Cu-rich fluid forms when sulfides decompose after a moderately H_2O-rich intermediate-composition magma has crystallized to a more silicic residual melt, similar to the scenario illustrated in Figure 6B. Complete decomposition of sulfide leads to wholesale transfer of Cu and Au to the early-saturating fluid phase, such that metal ratios in the fluid reflect those of the parent magma. This was observed at Bajo de la Alumbrera where Cu/Au of magmatic sulfides matches the same ratio in high-T brines and the bulk Cu/Au ratio of the deposit, indicating co-transfer and co-precipitation of Cu and Au (Ulrich et al., 2002; Halter et al., 2005). Platinum and Pd are even more chalcophile than Au, but equally soluble in Cl-bearing fluids at magmatic T (Simon and Pettke, 2009; Sullivan et al., 2022). Decomposition of any entrained magmatic sulfide is likely to transfer contained PGE's to the fluid, but they may require specific conditions to co-precipitate with Cu and Au in porphyry ores (Robb et al., 2023). Therefore, PGE depletion in magmatic rocks may not only be due to their sequestration into lower-crustal magmatic sulfides (cf. Cocker et al., 2015; Park et al., 2021).

V. The Hydrology and Duration of Fluid Extraction and Focusing

The physics of fluid extraction from an upper-crustal magma chamber

Figure 7 combines results from three finite-element – finite-volume studies exploring a mid-sized magma chamber, computed in 2 dimensions but scaled to a circular symmetry (Weis et al., 2012; Andersen and Weis, 2020; Lamy-Chappuis et al., 2020). Each study builds on the same Complex Systems Modeling code (CSPM+; Coumou et al., 2008), but none of the computations numerically couples all physical processes. Thus, Andersen and Weis (2020) compute magma transport within the magma chamber (which is ignored in Lamy-Chappuis et al, 2020), to explore the impact of T-induced convection on the rate of heat loss and the crystallization lifetime, but they do not compute the saturation of fluid bubbles, nor simulate the interplay between convection, exsolution and transport of exsolved fluid bubbles (cf. Cloos, 2001), as an alternative or complement to fluid focussing by tube flow (Parmigiani et al., 2011). Results of each simulation are sensitive to assumed bulk material properties expressed in simple empirical functions, such as porosity-dependent 'relative permeabilities' for liquid and vapor as a function of fluid overpressure (to mimic hydraulic fracturing) and temperature (to mimick the brittle-ductile transition of rocks that tends to close permeability at higher T; Weis et al., 2012). Bulk permeability of magma as a function of melt:crystal:fluid ratio varies with advancing crystallization and fluid expulsion (Lamy-Chappuis et al., 2020). A rather low initial H_2O content of the melt (2.5 wt%) was used in this study. A more realistic H_2O content >4% is expected to shift the high-permeability tube-flow behavior to lower melt:crystal fractions, but parameter limits have not been explored. Some aspects of the results are predicated by geological observations, e.g., Cu is assumed to precipitate between 450 and 350 °C based on Landtwing et al. (2010). Therefore, the mass-balance and the tendency of Cu accumulation along a downward-retracting T-front is a robust conclusion of Weis et al. (2012), but the absolute T at which this occurs is less certain (cf. Cernuschi et al., 2023). Aspects of the size and depth of magma chambers and the location of the fluid focussing point have been explored by modifying geometric assumptions (Lamy-Chappuis et al., 2020), and the influence of zones of higher permeability in the hydrostatically-pressured wall-rock domain were studied by Codeço et al. (2022), but their coupling to predict the location of magmatic-hydrothermal focusing has not yet been simulated. Filling of the magma chamber is assumed to be instantaneous. Korges et al. (2020) computed the effect of successive sill-like filling of a magma chamber, which extends the life-time of the magma chamber, but this time extension is modest, so long as the succession of filling events is fast enough to generate a coherent mush volume allowing efficient fluid extraction.

The numerical models for mass- and heat conservation and resulting fluid flow and focussing are physically rigorous for the stated assumptions, and they correctly predict changing fluid properties including single- and two-phase state of NaCl-H_2O model fluids as a function of P and T, supporting the interpretation of fluid inclusions in Figure 10. However, they are limited by boundary conditions and simplified descriptions of rock and magma behaviour that each model considers.

Mafic underplating as a trigger to hydrothermal fluid generation

Injection of mafic magma is known as a trigger to volcanic eruptions, by adding heat and CO_2 to more felsic magma reservoirs (Sparks et al., 1977; Bachmann et al., 2002). This is likely to apply also to the onset of ore fluid generation in some, perhaps many porphyry systems (Hattori and Keith, 2001; Wilkinson, 2013). Mineralized porphyries and associated (sub)volcanic rocks commonly show entrained mafic enclaves and evidence of mafic – felsic magma mixing in phenocryst melt inclusions (Halter et al., 2005; Zhang and Audétat, 2017). I may be criticized for not adequately reviewing this evidence and underestimating the role of selective component addition by mafic magmas to upper-crustal magma reservoirs (e.g., S for ore formation, discussed by Audétat and Pettke, 2006). Understanding and predicting the trigger to an active eruption is obviously essential for risk mitigation (Bachmann and Huber, 2016). However, understanding what determines the point in time when ore formation starts seems less important than understanding the longer-term and large-scale evolution creating a magma reservoir capable of generating a large, rapid but non-explosive flux of aqueous ore fluid (cf. seemingly conflicting evidence at Bingham Canyon, section II above). In other words, if the chain of processes emphasized in the main paper is valid and all essential steps are perfectly aligned in space and time in a particular geological setting, nothing will stop the formation of an ore deposit, no matter whether hydrothermal ore formation starts today or a year later.

Geochronology: methods, limitations, and interpretation of 'lifetimes'

The example of Bingham Canyon (Fig. 8B) explains the approach to geochronological bracketing used in the main Figure 8A, based on magma – vein – magma – vein intersections exemplified by Figure 8C (Large et al., 2021). Following the workflow of Chelle-Michou et al. (2014) and Samperton et al. (2015), single zircon grains were first analysed by LA-ICPMS for a suite of trace elements and then plucked out of the grain mount for CA-ID-TIMS dating. Results show a simple correlation between age, temperature determined by Ti-in-zircon thermometry, and trace element concentrations, indicating monotonous cooling and crystallization of one dominant magma as common source of 4 successive intrusions and the ore fluids. EM is an equigranular monzonite from the broadly exposed roof of an underlying batholith quantified by inversion of an aeromagnetic anomaly, which indicates a magma volume consistent with mass-balance requirements to form this giant ore deposit (Steinberger et al., 2013). The EM contains anhedral, texturally interstitial zircons whose Ti temperatures indicate rapid intrusion and in-situ crystallization of a hot and initially zircon-undersaturated melt with moderate H_2O content, similar to the scenario described in Figures 4C and 6B. QMP and LP are two porphyry intrusions followed each by intense quartz veining and Cu-introduction, after which the orebody volume was kept above ~350°C to prevent quartz-muscovite alteration and pyrite veining before the intrusion of the significantly younger QLP (Redmond and Einaudi, 2010). In Figure 8, the waning of Cu introduction is indicated by gradational yellow-to-gray shading, but its termination is unconstrained, as is the duration of late quartz-molybdenite veining postdating QLP (Fig. 8C). The interpretation of a single upper-crustal magma chamber forming Bingham has been tested by thermal modelling (Karakas et al., 2017), and the observed Ti-in-zircon *vs.* time variation can be explained by rapid filling of this magma chamber followed by slow monotonous cooling over ~800 ka, provided that the underlying crust was preheated by vertically extensive preceding intrusions (Large et al., 2021).

In constructing age brackets summarized in Figure 8, the youngest zircon in a porphyry sample dates, strictly speaking, the *maximum* age of emplacement and quenching of the groundmass, because the next analysed zircon grain might still be a little younger. For some porphyries at Bajo de la Alumbrera, Buret al. (2016) analysed a sufficiently large number of zircon micro-phenocrysts to obtain a 'plateau' of several youngest ages overlapping within small analytical error (± 10 ka), which convincingly date porphyry emplacement and rapid quenching of its groundmass. Most other CA-ID-TIMS studies report a smaller number of grain analysis, but assuming the youngest zircon as the time of porphyry emplacement is unlikely to disturb the broad correlation of durations with deposit tonnage (Fig. 8). The statistics of this error source has been investigated by Keller et al. (2018), and the role of analytical precision in this interpretation strategy was compared with other geochronometers by Chiaradia et al. (2013).

The biggest uncertainty of this approach to measuring process durations remains with geological interpretation. On one hand, the bracketing porphyry ages are subject to the question of the *youngest* zircon from each intrusion. On the other hand, the high-precision time bracket on intrusions only gives an *upper* limit on the duration of hydrothermal mineralization, which may well be significantly shorter. This is shown by one of the most careful Re-Os studies using geologically well-controlled molybdenite samples (Pollard et al., 2021), indicating durations of 10 – 40 ka for several discrete mineralization events at Ok Tedi. These short durations are in line with the age vs. tonnage sequence indicated by Figure 8 and with physical modelling (Fig. 7; see Large et al., 2018, for geological argumentation). The total range of molybdenite Re-Os ages from Ok Tedi is much wider, spanning ~200 ka between all mineralization phases including early skarn ore (Pollard et al., 2021). This implies that the range of Re-Os molybdenite ages without detailed geological control is not a good measure of the duration of mineralization, nor a good predictor of total metal tonnage. Results from Ok Tedi rather indicate several smaller mineralizing intrusions, consistent with the complex N-S-extended geometry of this deposit.

At El Teniente, the total range of Re-Os ages of ~ 0.8 Ma (Maksaev et al., 2004; Cannell et al., 2005; Spencer et al., 2015; excluding significantly older and younger samples outside the concentric ore shell) is similar to the reconnaissance dating of zircons shown in Figure 8, bracketing quartz and sulfide veining within ~ 0.6 Ma (Schumacher et al., 2018). The compilation of all molybdenite Re-Os dates (Spencer et al., 2015) shows clusters of Re-Os ages, but no apparent relation of inferred 'mineralization pulses' to distinct intrusive bodies, in contrast to observations at Ok Tedi by Pollard et al. (2021). The ICPMS-U-Pb ages of Schumacher (2018) fall into two groups with large scatter in each sample: (a) three separate Diorite intrusions that are predating and presumably causing most veining and Cu-Mo mineralization, and (b)

overlapping groups of Teniente Dacite Porphyry (interpreted as inter-mineral to late-mineral intrusion) and juvenile Latite clasts in the Braden Breccia Pipe (terminating the main economic mineralization). LA-ICPMS is not precise enough to determine individual youngest zircons but the age difference between the few youngest grains in sample group (a) and the few youngest grains in sample group (b) is ~600ka, and comparing the median results (a) and the median of (b) is also ~600ka. This consistent age bracket, with an estimated uncertainty of ± 100ka, is plotted as yellow interval in the left age column of Figure 6A, together with the oldest zircons in sample group (a) as its top — clearly an analytically poor, but geologically well supported bracket to the duration of hydrothermal mineralization at El Teniente. Geochronological data are therefore consistent with the first-order interpretation of the El Teniente ore shell as the product of one major hydrothermal event related to one giant magma reservoir.

High-precision CA-ID-TIMS results based on similar field constraints were obtained by at least two additional zircon studies that are not included in this diagram, either because of age ambiguity regarding a bracketing post-ore intrusion (Chelle-Michou et al., 2014) or the absence of an exposed first mineralizing porphyry, which is only indicated by dating of early molybdenite (Li et al., 2017). However, at least the latter results from Qulong (11 Mt Cu emplaced within 266 ka) fit well between Batu Hijau and Bingham Canyon on Figure 8 and further support the relationship between duration and Cu endowment in line with thermal constraints.

Diffusion chronometry of Ti zoning in hydrothermal quartz in the Butte porphyry Cu-Mo deposit has been suggested to indicate intermittent cooling between quartz precipitation pulses at 750-400°C on the 10ka time scale or faster (Mercer et al., 2015), which could potentially be related to the short pulsation predicted by mechanical feedbacks between permeability opening and closing (Weis et al., 2012). However, the extrapolation of diffusion constants from high-T experiments to hydrothermal conditions has later been revised (J. Dilles, pers. comm, 2023), and new results from the Haquira East deposit (Peru) permit monotonous cooling from magmatic T to <350°C in ~ 10^5 years, with most ore deposition completed within 35 ka (Cernuschi et al., 2018), in line with the zircon geochronology of other medium-sized deposits shown in Figure 8.

VI. Vein formation, ore deposition and wall-rock alteration

This section of the main paper attempts to explain the most common features of porphyry Cu-Mo-Au deposits with a simplified interpretation of the range of fluid processes. I try to present an intuitive explanation that acknowledges dissenting interpretations but is not weighed down by the vast body of published deposit-specific observations including extensive fluid-inclusion data, nor by an extended review of the large experimental database underlying my interpretation. Here I add some experimental background, explanation of my terminology, a summary of underlying fluid inclusion observations with some extra references and additional comments on deviating interpretations.

Experimental background: NaCl-H_2O model system

Figure 10 of the main paper is a cartoon depicting magmatic fluid evolution based on density and salinity variations in the NaCl-H_2O model system, which were defined by a large number of experimental studies and are depicted in the projected P –T – X_{NaCl} phase diagram below (Driesner, 2007; Driesner and Heinrich, 2007; with earlier references). The two-phase surface (liquid + vapor coexistence or solvus in the binary system) is shown by the black upward-convex grid. The red curve extends the boiling curve of pure water between 0 and 374°C (the critical point of pure water = red dot) to the critical curve in the binary system at higher P and T, defining the highest pressure at which two fluids of different salinity can coexist. The 3-phase surface (practically salt-free H_2O vapor + maximum-salinity brine + halite $NaCl_{solid}$) is indicated by 3 green lines, defining a horizontal cylindrical volume at low P, below which practically salt-free H_2O vapor + halite coexist.

Arrows through the phase diagram (A to D), and corresponding changes in fluid properties with depth in Figure 10A to 10D, are shaded with a schematic blue-white-black color scheme, according to the approximate graphical scale for fluid density (darkness) and salinity (blue-ness), as shown by the inset to the right (modified from Williams-Jones and Heinrich, 2005; Heinrich and Candela, 2014).

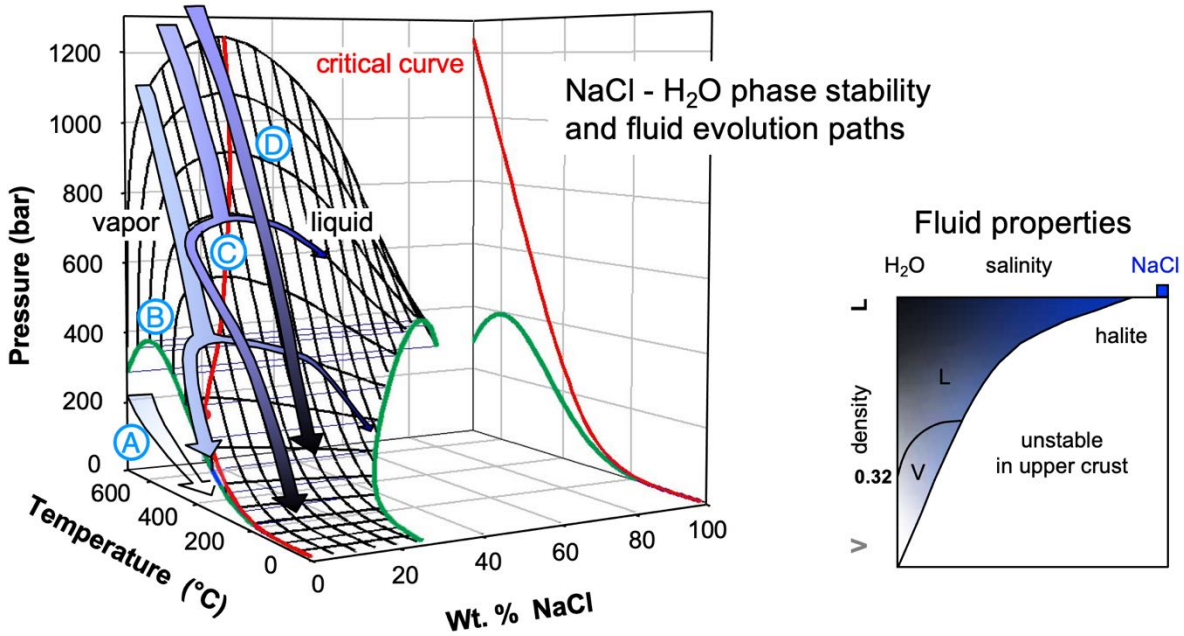

Terminology for describing fluid evolution and inclusions

The terminology for changes in phase property within the single-phase field (variation of density) and for transitions between one and two-phase states by crossing of a phase boundary (separation into more NaCl-rich liquid and more H_2O-rich vapor) allows description of deposit-scale fluid evolution as well as changes observed during microthermometry of fluid inclusions (Liebscher and Heinrich, 2007). In the main paper I use terms that are analogous to those applicable to pure water. Thus, a change from a homogeneous single-phase state to coexisting liquid + vapor can occur in two ways (Henley and McNabb, 1978). It either occurs by *condensation* or *droplet formation,* if the two-phase surface is intersected from the vapor side, and the same term is used when a vapor-like fluid intersects the binary solvus on its low-salinity side (i.e., to the left of the red critical curve in the phase diagram above), as shown by paths A, B and C. The resulting fluid evolution is illustrated in Figure 10A to 10C, respectively. Alternatively, *boiling or bubble-formation* occurs if the 2-phase boundary is intersected on the liquid side (pure H_2O at 100°C and atmospheric pressure), which in the binary system corresponds to intersection of the solvus on the high-salinity side of the red critical curve on the black-gridded surface. These two processes were originally described with reference to dew-point and bubble-point curves in P-T projections to explain fluid inclusions in magmatic-hydrothermal ore deposits and sea-floor hydrothermal systems (Roedder, 1984; Bischoff and Pitzer, 1989; Bodnar, 1995) and seem to me more fundamental to understanding fluid evolution than the somewhat semantic distinction between 'boiling' in a single-component system from 'unmixing' in a multicomponent fluid system.

Changes in phase property within the single-phase field are iso-chemical by definition, and either involve *expansion* (decrease in fluid density) or *contraction* (increase in fluid density). A particular feature of the NaCl-H_2O system is its asymmetric solvus in P-T-X space, causing the critical curve to swing to higher salinity with increasing P and T above the critical endpoint of the H_2O system.

The term 'brine' is loosely used for an aqueous liquid with a salinity above halite saturation at room temperature (~26 wt%), thus precipitating a halite crystal when a brine inclusion is cooled to ambient temperature. With additional salt components including KCl and $FeCl_2$, brines may have even higher Cl/H_2O ratio than in the binary NaCl-H_2O system, extending all the way to pure NaCl-KCl-$FeCl_2$ salt melts without detectable H_2O, as observed in some porphyry-Au deposits (Koděra et al., 2014). Anhydrous salt melts are stable below the melting temperature of halite (~800°C) and then take the position of solid halite in the binary model system at high T but low P.

I generally use 'vapor' for any fluid of low density coexisting with a denser liquid or brine, and 'vapor-like' for a fluid with lower density than the critical density of the given composition in the single-phase

stability field. The term 'gas' is occasionally used for a vapor phase at atmospheric pressure, following the widespread usage in the volcanic gas literature (Giggenbach, 1992). I avoid the term 'supercritical', which has no unambiguous definition in multicomponent systems, and instead prefer the description of a fluid in the single-phase stability field (Liebscher and Heinrich, 2007).

Fluid evolution paths in magmatic-hydrothermal systems: fluid inclusion evidence

The four P-T paths in the phase diagram and the four illustrations of Figure 10 interpret alternative evolutions of low-salinity fluids between the point of exsolution from magma to the Earth's surface, based on interpretations of fluid inclusion observations.

Depth to magma, the salinity of the magmatic starting point and the curvature and intersection points of the four paths are schematic, but all are based on fluid inclusion observations in different porphyry – epithermal ore systems and are physically plausible based on hydrodynamic modeling. Path C, in particular shows a low-salinity magmatic fluid first intersecting the two-phase curve on the vapor side (condensing brine droplets), followed by selective escape of the dominant lower-density and less-viscous vapor into a cooler domain at elevated pressure. This path results from the strong cooling gradient at the periphery of a porphyry-mineralizing fluid plume (Weis et al., 2012). Contraction of this magmatic vapor to an aqueous liquid of the same low salinity crosses above the critical curve from vapor-like density to liquid-like density (low-salinity branch of the bifurcating path B in the P-T-X diagram above, shown by cartoon Fig. 10B). This evolution is recorded by fluid inclusion associations in many low- to intermediate-sulfidation epithermal ore deposits, as compiled in figure 2 of Heinrich (2005). They show a main trend of low-salinity liquid inclusions with densities between near-critical (homogenization temperature T_h~400°C) and liquid (T_h~300-150°C), and secondary near-isothermal trends, sometimes even within one fluid inclusion assemblage, towards more saline inclusions of randomly variable salinity up to that of distinct brine inclusions with 30-50 wt% $NaCl_{eq}$. Some of these studies include fluid inclusions in enargite (see also Piperov et al., 2017) and from quartz-sericite-pyrite veins underlying and grading up into a high-sulfidation epithermal deposits (e.g., Rodalquilar, Spain, Arribas et al., 1995). The two inclusion trends in the same samples indicate that such epithermal deposits form from a dominant low-salinity aqueous liquid at temperatures below the critical point of water (374°C). Here, the contracted low-salinity magmatic liquid is miscible with heated meteoric water and may boil by separation of essentially salt-free low-density vapor (indicated by small-bubbled liquid inclusions, trapped together with essentially empty vapor inclusions; inset photomicrograph near the top of Fig. 10C; Baja Sprie, Romania). The second trend to variably saline brines shows that minor magmatic fluid is locally entrained by the dominant vapor-derived magmatic liquid (e.g., Nansatsu, Japan, Hedenquist et al., 1994; Chinkuashih, Taiwan, Wang et al., 1999). The two trends together indicate that the low-salinity epithermal liquid in these deposits is not an unmodified magmatic fluid that never intersected the NaCl-H_2O solvus (path D), but has intersected the two-phase surface at greater depth to condense high-salinity brine, before cooling and contraction of the dominant vapor phase to epithermal liquid (Path C). Vapor contraction and renewed miscibility with liquids (magmatic brine as well as meteoric water) are both shown by these fluid inclusion data, but energy balance may require that contraction and mixing of high-enthalpy magmatic with low-enthalpy meteoric water proceed together. These thermal constraints have not yet been fully explored.

The evidence for brine separation at greater depth below epithermal deposits has consequences for the chemical separation of metals on the way from magma to surface. Upon phase separation, Cu, Fe and Cl will preferentially remain in the liquid phase or directly combine with S to Cu-Fe-sulfides and pyrite in the domain of brine + vapor coexistence (Lerchbauer and Audétat, 2012, correcting the erroneous interpretation of vapor inclusion analyses by Heinrich et al., 1999, which requires modification of the input assumptions for multicomponent reaction modeling in Heinrich, 2005). By contrast, ppm-levels of Au in porphyry vapor inclusions (Ulrich et al., 1999) are unlikely to be artefacts of post-entrapment Au diffusion into fluid inclusions (Seo and Heinrich, 2013), and experiments show that Au remains soluble in a H_2S-rich low-salinity aqueous fluid from 50 MPa / 500°C down to subcritical temperatures (Stefánsson and Seward, 2004), so long as H_2S is not removed by reaction with Fe to form pyrite (confirming the calculations in Heinrich et al., 2004). Thus, brine separation at depth favors the transport of high concentrations of S-complexed Au to epithermal temperatures, as low as those involved in Carlin-type ore formation (<200°C; Large et al., 2016). Alternatively, boiling of the low-salinity liquid at near-surface pressures promotes Au precipitation by H_2S loss, to create bonanza levels in epithermal gold veins (e.g.,

Shimizu, 2014). A fluid inclusion study of the Famatina (Argentina) ore field links the porphyry Cu-Mo environment through transitional quartz-sericite-pyrite veins to high-sulfidation epithermal Au-Cu-As ore (Pudack et al., 2009). Detectable Au together with high S concentrations in excess over Fe, were also found in low-salinity aqueous inclusions of the Alto de la Blenda gold veins (Farallón Negro, postdating the nearby Bajo de la Alumbrera porphyry Cu-Au deposit, Argentina; Márquez-Zavalía and Heinrich, 2016). These data are near the limit of LA-ICPMS microanalysis but, together with breccia fragments introduced into the epithermal vein system containing intermediate-density and vapor inclusions together with rare brine inclusions, are consistent with thermodynamic modeling and compiled inclusion data in Heinrich (2005).

Predicted effects of co-precipitating *vs.* separating Au from Cu in porphyry systems are indicated with orange and red labels in Figure 10, but the actual presence or absence of Au mineralization of course depends, first of all, on the initial Au content of the magmatic fluid and hence on the origin and fractionation history of the mineralizing magma.

Multicomponent thermodynamic reaction modeling

The calculation of multicomponent – multiphase chemical equilibrium combining diverse experimental thermodynamic data is a powerful tool to identify the dominant among competing chemical reactions affecting ore deposition. It also allows testing of multicomponent fluid-rock reaction against mass-balance measurements based on analysing hydrothermally altered and metal-enriched rocks in comparison with interpreted unaltered protolith rocks. For example, mass-balance analysis has quantified bulk reactions showing how SO_2 becomes reduced to H_2S by reaction with $FeCl_2$ to precipitate abundant hydrothermal magnetite during potassic alteration of dacite porphyry in the core of many porphyry deposits (Ulrich and Heinrich, 2002). It would be interesting to calculate how this reaction competes with the precipitation of anhydrite by SO_2 disproportionation and plagioclase decomposition (Henley et al., 2015) and how the additional H_2S influences the temperature of Cu-Fe-sulfide deposition. Multicomponent thermodynamic modelling of fluid-rock reaction in porphyry deposits remains limited, however, until we have a unified thermodynamic description of solute and solvent behavior spanning the range from highly saline liquids to low density vapor, including two-phase coexistence (Driesner, 2013; Seward et al., 2014).

As a result of this limitation, one group of published thermodynamic models extrapolates equations describing species properties in aqueous liquids to their limits near the critical density of H_2O, making activity adjustments for highly saline fluids (Helgeson et al., 1981; Akinfiev and Diamond, 2003). Several studies using this type of modeling emphasize the steep T-dependence of sulfide solubility in contact with reactive rocks (Crerar and Barnes, 1976; Hezarkhani and Williams-Jones, 1998) but predict different T of bornite and chalcopyrite saturation depending on their preference of thermodynamic data and their assumptions of the initial Cu concentration in the fluid (Heinrich, 2005; Kouzmanov and Pokrovski, 2012; Reed et al., 2013; Fontboté et al., 2017). These ambiguities prevent rigorous assessment of conflicting interpretations of the temperature of Cu-Fe-sulfide deposition (Schirra et al., 2022; Cernuschi et al., 2023; below). The other group of models addresses metal precipitation from gas-like fluids, emphasizing the strong dependence of mineral solubility on fluid density, including ore-metal separation (e.g., Au/Cu) resulting from variation in P_{fluid} (Migdisov et al., 2014; Henley and Seward, 2018; Hurtig et al., 2021). Apart from ignoring phase separation and the common coexistence of high-salinity liquid fluids, gas-based thermodynamic models are limited by fluid components for which no experimental volatility data are available – notably $FeCl_2$ as a major reactive component of low- to intermediate-density magmatic fluids.

Alternative interpretations and open questions — further comments

Whether brine and vapor physically separate from each other or flow together through the porphyry vein network depends on many unknown factors, notably the geometry of fracture paths and the local flow rate within each fracture. Local flow velocity is inherently faster than the average flow rate of vapor and liquid through fractured rock at deposit scale, as approximated by the simple concept of relative permeabilities (Weis et al., 2012). If the two fluids travel together, they will recombine after cooling to P-T conditions where they become miscible again, as inferred from fluid inclusion data at Batu Hijau (Schirra et al., 2022). If they separate from each other (e.g., due to preferential wetting of vein rocks by the liquid and/or lower density and viscosity of the vapor), Cl-complexed metals (Cu, Fe, part of the Au depending

on P-T conditions) preferentially remain in the brine, while the vapor removes more volatile components (H_2S, SO_2, As, B and sulfide-complexed Au). Even brine inclusions are high in total S according to fluid inclusions analyses (Seo et al., 2009) but most of this S is present as sulfate (SO_4^{2-}) in relatively oxidized porphyry brines (Pokrovski and Dubessy, 2015). Sulfide limitation in the brine phase is consistent with the observation that residual brines in porphyry Cu veins cooling to T<300°C remain constantly rich in Pb and Zn (comparable to Cu concentrations at higher T; Kouzmanov and Pokrovski 2012). High Pb/Cl and Zn/Cl indicate that sulfide exhaustion after Cu-Fe-sulfide precipitation at T> 300°C suppresses saturation with galena or sphalerite at lower T (Heinrich, 2006). Even Cu-rich brine by itself is probably not a good agent for high-grade ore formation but requires sulfide from coexisting and possibly re-homogenizing magmatic vapor (Schirra et al., 2022). The experiment-based suggestion that porphyry ore might be formed by large-scale later addition of H_2S-SO_2-rich vapor to previously accumulated Cu-rich brine (Blundy et al., 2015) lacks convincing geological evidence.

Mavrogenes et al. (2010) and Henley et al. (2012) have proposed that high-sulfidation gold deposits including El Indio and Summitville formed at >650°C from expanding magmatic gas, condensing an As-Sb-Bi-Sn-Pb-Tl-(-Au)-rich sulfidic melt. This interpretation is mainly based on high-temperature experiments and the interpretation of mineral reaction textures as products of subsolidus exsolution from high-T melt. Analytical evidence that these sulfide textures originated as homogeneous melts of constant but non-stoichiometric composition (e.g., by bulk LA-ICPMS analyses of complete inclusions in quartz) has not been published to my knowledge. Therefore, the myrmekite-like textures may equally be subsolidus reaction products among minerals that were co-precipitated at epithermal temperatures.

Molybdenum precipitation is neglected in my simplified interpretation of fluid evolution in porphyry systems. Molybdenite can be deposited before Cu-Fe-sulfides (Yulong: Chang et al., 2018; Jensen et al., 2022) or be distributed together with Cu in space and time (Los Pelambres: Perello et al., 2012), but most commonly is added late in the vein sequence, occurring either in deeper and inner parts of zoned orebodies (e.g., Butte, Bingham; Fig.9E) or outside of the best Cu grades extending into volcanic host rocks (e.g., Bajo de la Alumbrera; Proffett, 2003). Molybdenite at Bingham Canyon is concentrated in a distinct vein set postdating the last and most fractionated porphyry phase (Porter et al., 2012). Seo et al. (2012) found that these late fluids have Mo/Cu ratios indistinguishable from those generating earlier Cu-Au-ore and suggested that chemical competition of Mo for limited sulfide available in more acidic and reduced late-exsolving fluids suppressed chalcopyrite precipitation in the quartz-molybdenite veins. Jensen et al. (2022) on the other hand identified a specifically Mo-rich fluid at an intermediate stage of vein evolution at Escondida. Mo/Cu is particularly high in the Kisladag porphryry Au deposit, which was tentatively related to the alkaline magmas and a pre-history of earlier subduction metasomatism of the subcontinental lithospheric mantle (Baker et al., 2016). In addition, precipitation of molybdenite appears to be favored by very shallow mineralization depth, as indicated by the presence of molybdenite in sublimates of high-temperature fumaroles at (~500°C; Africano et al., 2002; Tessalina et al., 2008).

Supplementary References

Ahmad, I., Richards, J. P., Pearson, G. D., Liu, J., Barnes, S.-J., Jugo, P. J., Shah, M. T., Leubourne, M., and Jagoutz, O., 2021, Fractionation of sulfide phases controls the chalcophile metal budget of arc magmas: Evidence from the Chilas Complex, Kohistan arc, Pakistan: Society of Economic Geologists Special Publications, v. 24, 2, p. 297-310.

Archer, C., and Vance, D., 2008, The isotopic signature of the global riverine molybdenum flux and anoxia in the ancient oceans: Nature Geoscience, v. 1, p. 597-600.

Arnold, G. L., Lyons, T. W., Gordon, G. W., and Anbar, A. D., 2012, Extreme change in sulfide concentrations in the Black Sea during the Little Ice Age reconstructed using molybdenum isotopes: Geology, v. 40, p. 595-598.

Arribas, A., Cunningham, C. G., Rytuba, J. J., Rye, R. O., Kelly, W. C., Podwysocki, M. H., Mckee, E. H., and Tosdal, R. M., 1995, Geology, geochronology, fluid inclusions, and isotope geochemistry of the Rodalquilar gold alunite deposit, Spain: Economic Geology, v. 90, p. 795-822.

Audétat, A., 2019, The metal content of magmatic-hydrothermal fluids and Its relationship to mineralization potential: Economic Geology, v. 114, p. 1033-1056.

Audétat, A., and Pettke, T., 2006, Evolution of a porphyry-Cu mineralized magma system at Santa Rita, New Mexico (USA): Journal of Petrology, v. 47, p. 2021-2046.

Bachmann, O., Dungan, M. A., and Lipman, P. W., 2002, The Fish Canyon magma body, San Juan volcanic field: Rejuvenation and eruption of an upper-crustal batholith: Journal of Petrology, v. 43, p. 1469-1503.

Bischoff, J. L., and Pitzer, K. S., 1989, Liquid-Vapor Relations for the System Nacl-H_2O - Summary of the P-T-X Surface from 300°C to 500°C: American Journal of Science, v. 289, p. 217-248.

Blundy, J., Mavrogenes, J., Tattitch, B., Sparks, S., and Gilmer, A., 2015, Generation of porphyry copper deposits by gas-brine reaction in volcanic arcs: Nature Geoscience, v. 8, p. 235-240.

Bookstrom, A. A., Carten, R. B., Shannon, J. R., and Smith, R. P., 1988, Origins of bimodal leucogranite-lamprophyre suites, Climax and Red Mountan porphyry molybdenum systems, Colorado – petrologic and strontium isotopic evidence: Colorado School of Mines Quarterly, v. 83, p. 1-24.

Breillat, N., Guerrot, C., Marcoux, E., and Negrel, P., 2016, A new global database of d^{98}Mo in molybdenites: A literature review and new data: Journal of Geochemical Exploration, v. 161, p. 1-15.

Buret, Y., von Quadt, A., Heinrich, C. A., Selby, D., Wälle, M., and Peytcheva, I., 2016, From a long-lived upper-crustal magma chamber to rapid porphyry copper-emplacement: Reading the geochemistry of zircon crystals at Bajo de la Alumbrera (NW Argentina): Earth and Planetary Science Letters, v. 450, p. 120-131.

Campos, E. A., Touret, J. L. R., and Nikogosian, I., 2006, Magmatic fluid inclusions from the Zaldivar deposit, northern Chile: The role of early metal-bearing fluids in a porphyry copper system: Resource Geology, v. 56, p. 1-8.

Carten, R. B., White, W. H., and Stein, H. J., 1993, High-grade granite-related molybdenum systems: classification and origin: Geological Association of Canada Special Paper, v. 40, p. 521-5554.

Cernuschi, F., Dilles, J. H., Grocke, S. B., Valley, J. W., Kitajima, K., and Tepley, F. J., 2018, Rapid formation of porphyry copper deposits evidenced by diffusion of oxygen and titanium in quartz: Geology, v. 46, p. 611-614.

Chiaradia, M., 2020, Gold endowments of porphyry deposits controlled by precipitation efficiency: Nature Communications, v. 11, 1-10.

Chiaradia, M., Schaltegger, U., Spikings, R., Wotzlaw, J. F., and Ovtcharova, M., 2013, How accurately can we date the duration of magmatic-hydrothermal events in porphyry systems? Economic Geology, v. 108, p. 565-584.

Coumou, D., Matthäi, S., Geiger, S., and Driesner, T., 2008, A parallel FE-FV scheme to solve fluid flow in complex geologic media: Computers & Geosciences, v. 34, p. 1697-1707.

Cuney, M., 2010, Evolution of uranium fractionation processes through time: Driving the secular variation of uranium deposit types: Economic Geology, v. 105, p. 553-569.

Edmonds, M., and Mather, T. A., 2017, Volcanic sulfides and outgassing: Elements, v. 13, p. 105-110.

Georgatou, A. A., and Chiaradia, M., 2020, Magmatic sulfides in high-potassium calc-alkaline to shoshonitic and alkaline rocks: Solid Earth, v. 11, p. 1-21.

Ghiorso, M. S., and Gualda, G. A. R., 2015, An H_2O-CO_2 mixed fluid saturation model compatible with rhyolite-MELTS: Contributions to Mineralogy and Petrology, v. 169, 30p.

Gion, A. M., Gaillard, F., Freslon, N., Erdmann, S., and Di Carlo, I., 2022, A method for the direct analysis of quenched, magmatic-hydrothermal fluids recovered from high-pressure, high-temperature experiments: Chemical Geology, v. 609, 121061, 13p.

Greaney, A. T., Rudnick, R. L., Gaschnig, R. M., Whalen, J. B., Luais, B., and Clemens, J. D., 2018, Geochemistry of molybdenum in the continental crust: Geochimica et Cosmochimica Acta, v. 238, p. 36-54.

Haar, L., Gallagher, J. S., and Kell, G. S., 1984, NBS/NRC Steam Tables, London, Taylor & Francis.

Hannah, J. L., Stein, H. J., Wieser, M. E., de Laeter, J. R., and Varner, M. D., 2007, Molybdenum isotope variations in molybdenite: Vapor transport and Rayleigh fractionation of Mo: Geology, v. 35, p. 703-706.

Hedenquist, J. W., Matsuhisa, Y., Izawa, E., White, N. C., Giggenbach, W. F., and Aoki, M., 1994, Geology, geochemistry, and origin of high sulfidation Cu-Au mineralization in the Nansatsu District, Japan: Economic Geology, v. 89, p. 1-30.

Heinrich, C. A., Driesner, T., Stefánsson, A., and Seward, T. M., 2004, Magmatic vapor contraction and the transport of gold from the porphyry environment to epithermal ore deposits: Geology, v. 32, p. 761-764.

Heinrich, C. A., 2006, From fluid inclusion microanalysis to large-scale hydrothermal mass transfer in the Earth's interior: Journal of Mineralogical and Petrological Sciences, v. 101, p. 110-117.

Helgeson, H. C., Kirkham, D. H., and Flowers, G. C., 1981, Theoretical prediction of the thermodynamic behavior of aqueous-electrolytes at high-pressures and temperatures. 4. Calculation of activity-coefficients, osmotic coefficients, and apparent molal and standard and relative partial molal properties to 600°C and 5 kb: American Journal of Science, v. 281, p. 1249-1516.

Henley, R. W., and Seward, T. M., 2018, Gas-solid reactions in arc volcanoes: ancient and modern: Reviews in Mineralogy and Geochemistry, v. 84, p. 309-349.

Henley, R. W., Mavrogenes, J., and Tanner, D., 2012, Sulfosalt melts and heavy metal (As-Sb-Bi-Sn-Pb-Tl) fractionation during volcanic gas expansion: the El Indio (Chile) paleo-fumarole: Geofluids, v. 12, 199-215

Hennings, S. K., Wagner, T., Ulmer, P., and Heinrich, C. A., 2017, Fluid evolution of the Monte Mattoni mafic complex, Adamello Batholith, Northern Italy: insights from fluid Inclusion analysis and thermodynamic modeling: Journal of Petrology, v. 58, p. 1645-1670.

Hin, R. C., Hibbert, K. E. J., Chen, S., Willbold, M., Andersen, M. B., Kiseeva, E. S., Wood, B. J., Niu, Y. L., Sims, K. W. W., and Elliott, T., 2022, The influence of crustal recycling on the molybdenum isotope composition of the Earth's mantle: Earth and Planetary Science Letters, v. 595, 1-11.

Keller, C. B., Schoene, B., and Samperton, K. M., 2018, A stochastic sampling approach to zircon eruption age interpretation: Geochemical Perspectives Letters, v. 8, p. 31-35.

Kendall, B., Dahl, T. W., and Anbar, A. D., 2017, Good Golly, Why Moly? The stable isotope geochemistry of molybdenum, Reviews in Mineralogy & Geochemistry, v. 82, p. 683-732.

Korges, M., Weis, P., and Andersen, C., 2020, The role of incremental magma chamber growth on ore formation in porphyry copper systems: Earth and Planetary Science Letters, v. 552, p. 116584, 13p.

Large, R. R., Halpin, J. A., Danyushevsky, L. V., Maslennikov, V. V., Bull, S. W., Long, J. A., Gregory, D. D., Lounejeva, E., Lyons, T. W., Sack, P. J., McGoldrick, P. J., and Calver, C. R., 2014, Trace element content of sedimentary pyrite as a new proxy for deep-time ocean-atmosphere evolution: Earth and Planetary Science Letters, v. 389, p. 209-220.

Larocque, A. C. L., Stimac, J. A., Keith, J. D., and Huminicki, M. A. E., 2000, Evidence for open-system behavior in immiscible Fe-S-O liquids in silicate magmas: Implications for contributions of metals and sulfur to ore-forming fluids: Canadian Mineralogist, v. 38, p. 1233-1249.

Lerchbaumer, L., and Audétat, A., 2013, The Metal Content of Silicate Melts and Aqueous Fluids in Subeconomically Mo Mineralized Granites: Implications for Porphyry Mo Genesis: Economic Geology, v. 108, p. 987-1013.

Li, S., Junkin, W. D., Gaschnig, R. M., Ash, R. D., Piccoli, P. M., Candela, P. A., and Rudnick, R. L., 2020, Molybdenum contents of sulfides in ancient glacial diamictites: Implications for molybdenum delivery to the oceans prior to the Great Oxidation Event: Geochimica Et Cosmochimica Acta, v. 278, p. 30-50.

Liebscher, A., and Heinrich, C. A., 2007, Fluid-fluid interactions in the Earth's lithosphere: Reviews in Mineralogy and Geochemistry, v. 65, p. 1-13.

Maksaev, V., Munizaga, F., McWilliams, M., Fanning, M., Mathur, R., Ruiz, J., and Zentilli, M., 2004, New chronology for El Teniente, Chilean Andes, from U-Pb,40 Ar/39 Ar, Re-Os, and fission-track dating: Implications for the evolution of a supergiant porphyry Cu-Mo deposit: Society of Economic Geologists, Special Publication, v. 11, p. 15−54.

Malfait, W. J., Seifert, R., Petitgirard, S., Mezouar, M., and Sanchez-Valle, C., 2014, The density of andesitic melts and the compressibility of dissolved water in silicate melts at crustal and upper mantle conditions: Earth and Planetary Science Letters, v. 393, p. 31-38.

Mao, W., Zhong, H., Yang, J. H., Liu, L., Fu, Y. Z., Zhang, X. C., Li, J., Zhang, L., Fan, H. F., Tang, Y. W., and Chen, X. C., 2023, Molybdenum cycling in Andean-type subduction and metallogenic implications: Mineralium Deposita, v. 58, p. 1263-1278.

Márquez-Zavalía, M. F., and Heinrich, C. A., 2016, Fluid evolution in a volcanic-hosted epithermal carbonate-base metal-gold vein system: Alto de la Blenda, Faralln Negro, Argentina: Mineralium Deposita, v. 51, p. 873-902.

Mavrogenes, J., Henley, R. W., Reyes, A. G., and Berger, B., 2010, Sulfosalt melts: evidence of high-temperature vapor transport of metals in the formation of high-sulfidation lode gold deposits: Economic Geology, v. 105, p. 257-262.

Mercer, C. N., Reed, M. H., and Mercer, C. M., 2015, Time scales of porphyry Cu deposit formation: Insights from titanium diffusion in quartz: Economic Geology, v. 110, p. 587-602.

Migdisov, A. A., Bychkov, A. Y., Williams-Jones, A. E., and van Hinsberg, V. J., 2014, A predictive model for the transport of Cu by HCl-bearing water vapour in ore-forming magmatic-hydrothermal systems: Implications for copper porphyry ore formation: Geochimica et Cosmochimica Acta, v. 129, p. 33-53.

Mutschler, F. E., Ludington, S., and Bookstrom, A. A., 1999, Giant porphyry-related metal camps of the world - a database: U. S. Geological Survey, Open-File Report, v. 99-556, p. 1-5; Excel files at https://pubs.usgs.gov/of/1999/of1999-1556/.

Piperov, N. B., Atanassova, R., Kotzeva, B. G., and Iliev, T., 2017, Reequilibrated fluid inclusions in enargite-luzonite from the Chelopech high-sulfidation Cu-Au epithermal deposit (Bulgaria): Neues Jahrbuch Fur Mineralogie-Abhandlungen, v. 194, p. 297-310.

Pokrovski, G. S., and Dubessy, J., 2015, Stability and abundance of the trisulfur radical ion S_3^- in hydrothermal fluids: Earth and Planetary Science Letters, v. 411, p. 298-309.

Pollard, P. J., Jongens, R., Stein, H., Fanning, C. M., and Smillie, R., 2021, Rapid formation of porphyry and skarn copper-gold mineralization in a postsubduction environment: Re-Os and U-Pb geochronology of the Ok Tedi mine, Papua New Guinea: Economic Geology, v. 116, p. 533-558.

Pudack, C., Halter, W. E., Heinrich, C. A., and Pettke, T., 2009, Evolution of magmatic vapor to gold-rich epithermal liquid: The porphyry to epithermal transition at Nevados de Famatina, Northwest Argentina: Economic Geology, v. 104, p. 449-477.

Robb, S. J., Boucher, B. M., Mungall, J. E., and Hanley, J. J., 2023, Platinum-group elements (PGE) in the New Afton alkalic Cu-Au porphyry deposit, Canadian Cordillera, II: PGE distribution and models for the hydrothermal coprecipitation of Co-Ni-Pd-Pt in pyrite: Frontiers in Earth Science, v. 11, 819109, 1-26.

Rusk, B. G., Reed, M. H., Dilles, J. H., Klemm, L. M., and Heinrich, C. A., 2004, Compositions of magmatic hydrothermal fluids determined by LA-ICP-MS of fluid inclusions from the porphyry copper-molybdenum deposit at Butte, MT: Chemical Geology, v. 210, p. 173-199.

Schumacher, I., Peytcheva, I., and von Quadt, A., 2018, Geochronology and trace element geochemistry of zircons in porphyry copper deposit El Teniente, Chile – Final Report including BSc Thesis, University of Zurich: ETH Research Collection, doi.org/10.3929/ethz-b-000663091, 119 p.

Scott, C., Lyons, T. W., Bekker, A., Shen, Y., Poulton, S. W., Chu, X., and Anbar, A. D., 2008, Tracing the stepwise oxygenation of the Proterozoic ocean: Nature, v. 452, p. 456-460.

Seo, J. H., and Heinrich, C. A., 2013, Selective copper diffusion into quartz-hosted vapor inclusions: Evidence from other host minerals, driving forces, and consequences for Cu-Au ore formation: Geochimica Et Cosmochimica Acta, v. 113, p. 60-69.

Shimizu, T., 2014, Reinterpretation of quartz textures in terms of hydrothermal fluid evolution at the Koryu Au-Ag deposit, Japan: Economic Geology, v. 109, p. 2051-2065.

Simon, A. C., and Pettke, T., 2009, Platinum solubility and partitioning in a felsic melt-vapor-brine assemblage: Geochimica Et Cosmochimica Acta, v. 73, p. 438-454.

Sparks, S. R. J., Sigurdsson, H., and Wilson, L., 1977, Magma mixing - mechanism for triggering acid explosive eruptions: Nature, v. 267, p. 315-318.

Steinberger, I., Hinks, D., Driesner, T., and Heinrich, C. A., 2013, Source plutons driving porphyry copper ore formation: Combining geomagnetic data, thermal constraints, and chemical mass balance to quantify the magma chamber beneath the Bingham Canyon deposit: Economic Geology, v. 108, p. 605-624.

Sullivan, N. A., Zajacz, Z., Brenan, J. M., Hinde, J. C., Tsay, A., and Yin, Y. W., 2022, The solubility of gold and palladium in magmatic brines: Implications for PGE enrichment in mafic-ultramafic and porphyry environments: Geochimica et Cosmochimica Acta, v. 316, p. 230-252.

Sun, W., Audétat, A., and Dolejs, D., 2014, Solubility of molybdenite in hydrous granitic melts at 800 degrees C, 100-200 MPa: Geochimica et Cosmochimica Acta, v. 131, p. 393-401.
Tessalina, S. G., Yudovskaya, M. A., Chaplygin, I. V., Birck, J. L., and Capmas, F., 2008, Sources of unique rhenium enrichment in fumaroles and sulphides at Kudryavy volcano: Geochimica et Cosmochimica Acta, v. 72, p. 889-909.
Ulrich, T., and Heinrich, C. A., 2002, Geology and alteration geochemistry of the porphyry Cu-Au deposit at Bajo de la Alumbrera (vol 96, pg 1719, 2001): Economic Geology, v. 97, p. 1361-1364.
Ulrich, T., Günther, D., and Heinrich, C. A., 1999, Gold concentrations of magmatic brines and the metal budget of porphyry copper deposits: Nature, v. 399, p. 676-679.
Wang, Y. S., Sasaki, M., Sasada, M., and Chen, C. H., 1999, Fluid inclusion studies of the Chinkuashih high-sulfidation gold-copper deposits in Taiwan: Chemical Geology, v. 154, p. 155-167.
Weingärtner, H., and Franck, E. U., 2005, Supercritical water as a solvent: Angewandte Chemie Int. Ed., v. 44, p. 2672 – 2692.
Westermann, S., Vance, D., Cameron, V., Archer, C., and Robinson, S. A., 2014, Heterogeneous oxygenation states in the Atlantic and Tethys oceans during Oceanic Anoxic Event 2: Earth and Planetary Science Letters, v. 404, p. 178-189.
Westra, G., and Keith, S. B., 1981, Classification and Genesis of Stockwork Molybdenum Deposits: Economic Geology, v. 76, p. 844-873.
White, W. H., Bookstrom, A. A., Kamilli, R. J., Ganster, M. W., Smith, R. P., Ranta, D. E., and Steininger, R. C., 1981, Character and origin of Climax-type molybdenum deposits, Economic Geology 75th Anniversary Volume, Society of Economic Geologiststs, p. 270-316.
Wille, M., Nebel, O., Pettke, T., Vroon, P. Z., Konig, S., and Schoenberg, R., 2018, Molybdenum isotope variations in calc-alkaline lavas from the Banda arc, Indonesia: Assessing the effect of crystal fractionation in creating isotopically heavy continental crust: Chemical Geology, v. 485, p. 1-13.
Zajacz, Z., Hanley, J. J., Heinrich, C. A., Halter, W. E., and Guillong, M., 2009, Diffusive reequilibration of quartz-hosted silicate melt and fluid inclusions: Are all metal concentrations unmodified?: Geochimica et Cosmochimica Acta, v. 73, p. 3013-3027.
Zhang, D., and Audétat, A., 2017, What caused the formation of the giant Bingham Canyon porphyry Cu-Mo-Au deposit? Insights from melt inclusions and magmatic sulfides: Economic Geology, v. 112, p. 221-244.
Zhang, J. B., Chang, J., Wang, R., and Audetat, A., 2022, Can post-subduction porphyry Cu magmas form by partial melting of typical lower crustal amphibole-rich cumulates? Petrographic and experimental constraints from samples of the Kohistan and Gangdese arc roots: Journal of Petrology, v. 63, p.1-22.